Circumstellar environment of Herbig Ae/Be stars as seen by the IOTA

Rafael Millan-Gabet, F. Peter Schloerb, Wesley A. Traub

Rafael Millan-Gabet, F. Peter Schloerb, Wesley A. Traub, "Circumstellar environment of Herbig Ae/Be stars as seen by the IOTA," Proc. SPIE 4006, Interferometry in Optical Astronomy, (5 July 2000); doi: 10.1117/12.390260

SPIE.

Event: Astronomical Telescopes and Instrumentation, 2000, Munich, Germany

The circumstellar environment of Herbig Ae/Be stars as seen by the IOTA

Rafael Millan-Gabet[a], F. Peter Schloerb[a] and Wesley A. Traub[b]

[a]Physics and Astronomy Dept.
University of Massachusetts at Amherst
Amherst, MA 01003, USA
[b]Harvard-Smithsonian CfA, 60 Garden St.
Cambridge, MA 02138, USA

ABSTRACT

We have conducted the first systematic study of Herbig Ae/Be stars using the technique of long baseline stellar interferometry. The Infrared Optical Telescope Array (IOTA) resolves the source of the near-infrared excess flux charateristic of these systems in 11 of the 15 stars observed. A close companion to MWC 361-A (18 mas separation) has been detected interferometrically for the first time. The visibility data has been interpreted within the context of four models which represent the range of plausible representations for the brightness of the excess emission: a Gaussian distribution, a narrow uniform ring, an accretion disk, and an infrared companion. We find that the large sizes measured by the interferometer, $0.5 - 5.9$ AU, essentially invalidate accretion disk models that had been previously used to explain the spectroscopic observations. Although a unique model can not be determined for each source due to limited spatial frequency coverage, the observed symmetry of the sources favors, for the ensemble of the data, models in which the circumstellar dust is distributed in spherical envelopes.

Keywords: Interferometer, IOTA, Herbig Ae/Be stars, infrared excess, cicumstellar dust, accretion disk, dust envelopes

1. THE HERBIG AE/BE STARS

The Herbig Ae/Be (HAEBE) stars are understood to be young stellar objects of intermediate mass ($1.5 < M/M_{\odot} < 10$).[1] Observationally, they are defined by spectral types B to F8 with emission lines, and the presence of infrared (IR) to sub-mm excess flux due to hot and cool dust. The pre-main sequence nature of HAEBE stars is now well established.[2–7] In contrast, the question of the geometrical distribution of the material which gives rise to the characteristic long wavelength excess, has remained controversial and is still the subject of considerable debate.[8–10]

In an influential paper (Ref.11, hereafter HSVK), the first systematic analysis of optical through mm-wave continuum spectral energy dustributions (SED) was carried out for a large sample of HAEBE stars. The SEDs with shapes $\lambda F_{\lambda} \sim \lambda^{-4/3}$ (Group I in the classification of HSVK) were succesfully modelled under the assumption that the IR excess arises in a reprocessing and actively accreting disk, provided that the accretion rates are relatively high ($6 \times 10^{-7} \leq \dot{M} \leq 8 \times 10^{-5}\, M_{\odot}\, yr^{-1}$) and that opacity holes of a few stellar radii exist in the inner region of the disk. However, the physical nature of these holes has remained difficult to interpret.[11,8] Moreover, the SEDs of most HAEBE stars can be explained equally well with extended dust envelopes,[12,13,8] or by a combination of both geometries.[14,10]

Clearly, one way to make progress toward this important question is to obtain observations of the near-IR emission with sufficient angular resolution to resolve the structure around the central star, in order to constrain the models not only with respect to the observed SEDs, but also with respect to the spatial distribution of the IR emission.

Further author information: (Send correspondence to R. Millan-Gabet)
R.M.G: Current affiliation: Harvard-Smithsonian CfA; E-mail: rmillan@cfa.harvard.edu
F.P.S: E-mail: schloerb@astro.umass.edu
W.A.T: E-mail: wtraub@cfa.harvard.edu

In *Interferometry in Optical Astronomy*, Pierre J. Léna, Andreas Quirrenbach, Editors,
Proceedings of SPIE Vol. 4006 (2000) • 0277-786X/00/$15.00

2. EXPERIMENTAL PROCEDURE

The observations described in this paper were carried out at the Infrared Optical Telescope Array (IOTA), a Michelson stellar interferometer located on Mount Hopkins, Arizona.[15] Observations were made in the near-IR H ($\lambda_0 = 1.65\mu m, \Delta\lambda = 0.30\mu m$) and K′ ($\lambda_0 = 2.16\mu m, \Delta\lambda = 0.32\mu m$) bands; and using two IOTA baselines, of lengths $B = 21$ m (North-South orientation) and 38 m (North-North East orientation).

In this experiment, interference is produced in the pupil plane, by combining the collimated and path-equalized beams at a beam splitter. The two outputs of the beam splitter are focused onto two separate pixels of a NICMOS3 detector, and a scan containing an intensity fringe packet is recorded at each pixel by modulating the OPD by $\pm 60\,\mu m$ via an extra reflection in one of the arms at a mirror mounted on a piezo stack. The OPD modulation is driven by a highly linear triangle waveform, at selectable rates in the range $1 - 10$ scans/sec. Figure 1 shows schematically the beam combination and fringe detection layout on the optical bench.

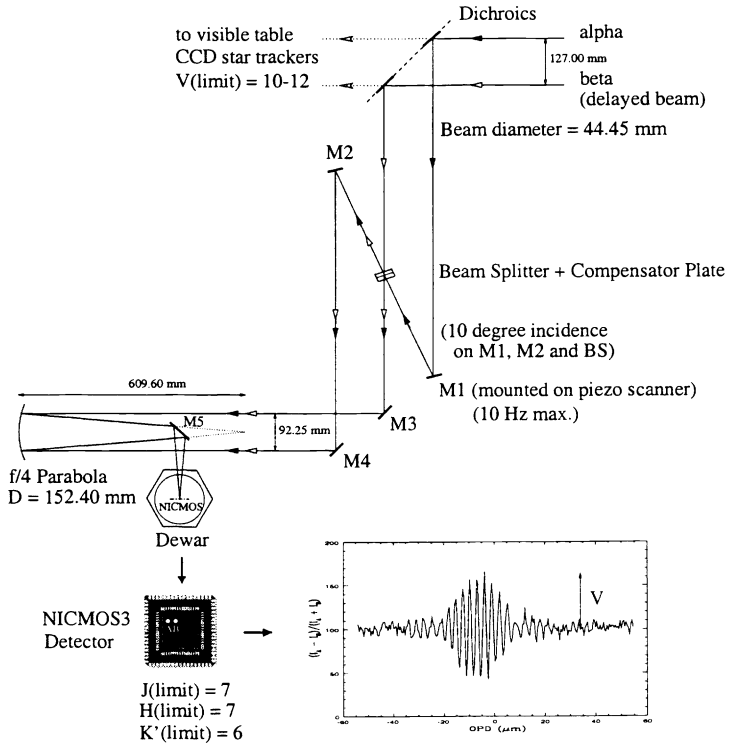

Figure 1. IR table optical layout.

Each scan contains 256 samples, with integration times per data point in the range $0.18 - 2.0\,ms$, chosen as the optimum in order to achieve maximum flux sensitivity while keeping the scan time short in order to freeze the wavefront piston fluctuations induced by the atmosphere during the fringe packet acquisition. With this detection system, the limiting magnitudes for real-time visual detection of a fringe packet in a single scan are 7 at H-band (read-noise limited) and 6.2 at K′-band (background limited), given here as the magnitudes of the faintest sources observed under typical conditions.[16,17]

A typical observation consists of 500 scans obtained in 1-8 mins, followed by 10 scans on the sky which are used to subtract the background flux. Target observations are interleaved with an identical sequence obtained on an unresolved star, which serve to calibrate the interferometer's instrumental response and the effect of atmospheric seeing on the visibility amplitudes. The target and calibrator sources are typically separated on the sky by a few degrees, and observed a few minutes apart; both of which insure that the calibrator observations provide a good estimate of the instrument's transfer function.

3. DATA REDUCTION AND ANALYSIS

Our procedure to obtain calibrated visibility amplitudes from the measured fringes consists of the following steps:

1. Fit the central fringes to the instrument's point-source response, in the time-domain, in order to obtain the visibility (fringe contrast) for each interferogram (V_i).
2. Fit the measured distribution of the V_i values in an observation ($i = 1, \ldots, n = 500$) to a model which incorporates the effects on the visibility of residual wavefront tip-tilt errors due to the atmosphere, as illustrated in Figure 2 (left panel). This step results in an estimate of the visibility for the observation (V).
3. Calibration of fixed instrumental terms using observations of unresolved sources, resulting in an estimate of the true target visibility given by V_{target}/V_{cal}.

We find that the use of the visibility distribution model (VDM, step 2) reduces the scatter in independent measurements of a given source under varying seeing conditions by factors of $2-3$, compared to more traditional estimators such as the mean of the measured distribution. This improvement is illustrated in Figure 2 (right panels), which compares both methods on data obtained on the same target on 4 nights of very different seeing conditions.

As can be seen in Figure 2 (top right panel), systematic differences larger than the internal errors from fitting the fringes and the VDM remain, likely due to residual calibration errors arising in un-modelled higher order wavefront errors. Thus, the error on an individual visibility measurement is best represented by the RMS of independent observations at similar spatial frequencies, and is typically of order 5%.

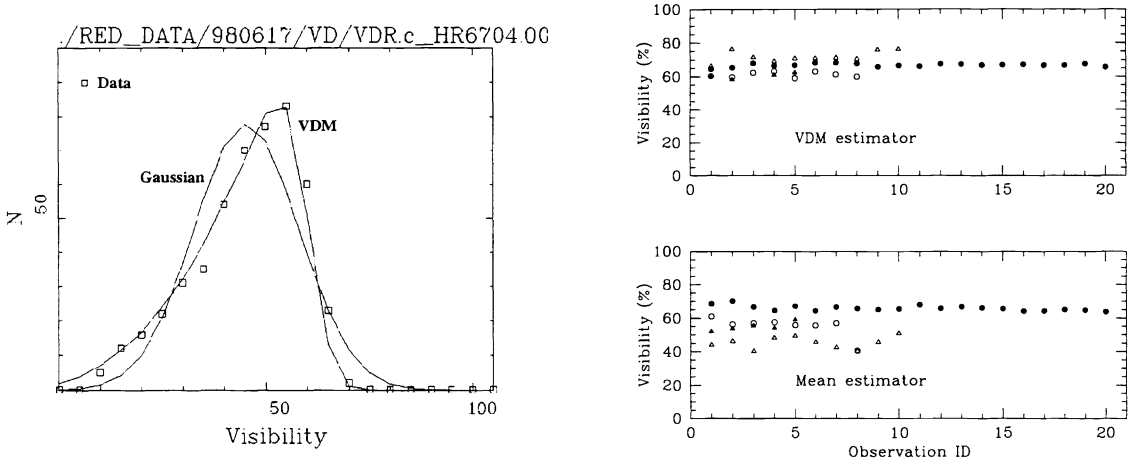

Figure 2. *Left panel*: Comparison of visibility data (V_i) in an observation (500 scans) with a Gaussian distribution and with the visibility distribution model (VDM). It can be clearly seen that the data distribution is not well represented by the Gaussian distribution, such that traditional estimators such as the mean would not be appropriate. In this case the visibility estimate given by the mean is $42.8 \pm 0.6\%$, while the estimate given by the VDM is $V = 60.9 \pm 0.3\%$. *Right panel*: Calibrated visibilities obtained using: the VDM (top panel) and the mean of the measured distribution (bottom panel). Each data point represents an observation of the same source (AB Aur) using identical detection parameters, and different symbols are used for different nights covering a large range of seeing conditions. For reference, the longest set of data (filled bullets) spans 5.2 hours.

4. OBSERVATIONS OF HAEBE STARS

The following points summarize the important characteristics of the sample selected:

- 15 HAEBE stars observed between October 1997 - March 1999.
- All are from Table 1 (bona fide HAEBES) in the catalog of Ref. 18.
- 13 are Group I of HSVK (SED shape: $\lambda F_\lambda \sim \lambda^{-4/3}$).
- 2 are Group III of HSVK (no or small IR excess).

Examples of the data obtained are shown in Figure 3. The following summarizes the important conclusions that may be drawn from the data set just based on inspection:

1. 11 of the 15 sources are resolved, the visibility amplitudes are in the range $50 \leq V < 100\%$.
2. 4 stars are unresolved: 3 Group I (V594 Cas, T Ori, MWC 147), and 1 Group III (ω Ori).
3. Of the 2 Group III stars in the sample, ω Ori appears unresolved and MWC 166 appears only slightly resoved, both consistent with that classification.
4. 1 source (MWC 361-A) shows the clear signature of a binary system.
5. Within the range covered by the observations, all other sources have approximately constant visibilities as the baseline orientation changes. This is indicative of sources which appear circularly symmetric on the sky.

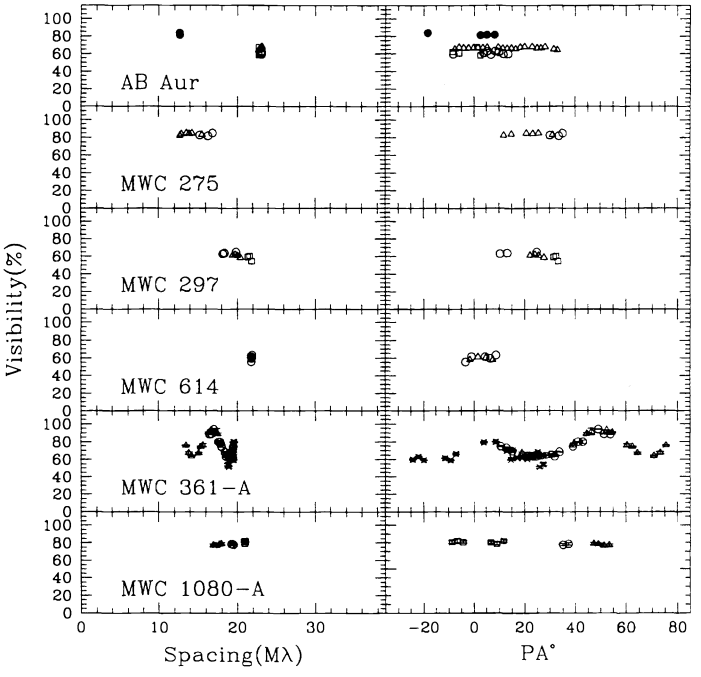

Figure 3. Examples of visibility data. Filled and open symbols indicate observations on the 21 m and 38 m baselines respectively. The data are plotted as a function of the projected baseline length (left panels) and position angle measured from North toward East (right panels). Each symbol represents observations on a different night. Note that the data for MWC 361-A clearly exhibits the sinusoidal signature of a binary system. Note also that for all other sources the visibility remains constant as the interferometer baseline changes orientation.

5. INTERPRETING THE VISIBILITY DATA

Most of the HAEBE stars in our sample are known to have a strong near-IR excess, and are resolved by the interferometer. Therefore, we consider a two component model consisting of the central star, plus a component which is the source of the near-IR excess. However, before this model can be used to interpret the interferometer data, the contributions to the total H and K fluxes from these two components must be determined.

5.1. Flux Decomposition

In order to estimate the stellar near-IR fluxes, we assume that the short wavelength flux arises entirely from the central star, and approximate the stellar spectrum as a blackbody at the adopted effective temperature from the literature. The solid angle (Ω) subtended by the stellar disk is the parameter adjusted in order to provide a best fit to the de-reddened V, R and I fluxes. Once the solid angle factor is thus determined, the stellar flux may be calculated at any wavelength. This procedure also allows us to estimate the angular sizes for the central stars, $\theta^\star = 2\sqrt{\Omega/\pi}$, with the result that in all cases they are small compared to the resolution of the interferometer, and implying that it is the source of the excess emission which the interferometer resolves. Using this model to represent the stellar photosphere, we deduce the apparent excess fluxes due to CS emission at the H and K bands of the interferometric observations, by subtracting the stellar fluxes from the measured total fluxes from the literature.

We find that the apparent excess fluxes represent $12-84\%$ of the total flux at H (58% average) and $31-94\%$ at K (78% average). Moreover, for all the Group I sources, the fraction of total flux in the central stars is well below the measured visibilities, indicating that our data is consistent with a partially, but not fully, resolved CS component.

5.2. Source Models

For all our resolved sources, we consider four plausible models of the source brightness. Each model has two components, with the stellar emission arising in a central point source and the excess near-IR emission contributed by either: (1) a Gaussian brightness distribution, (2) a uniformly bright ring, (3) a "classical" accretion disk with a temperature law $T(r) \propto r^{-3/4}$ or (4) an infrared companion. In all cases, the second component is constrained by the requirement that its flux matches the measured H and K excess fluxes. Both the Gaussian and ring models are assumed to appear circularly symmetric on the sky, consistent with the observed lack of visibility variations with baseline position angle (PA).

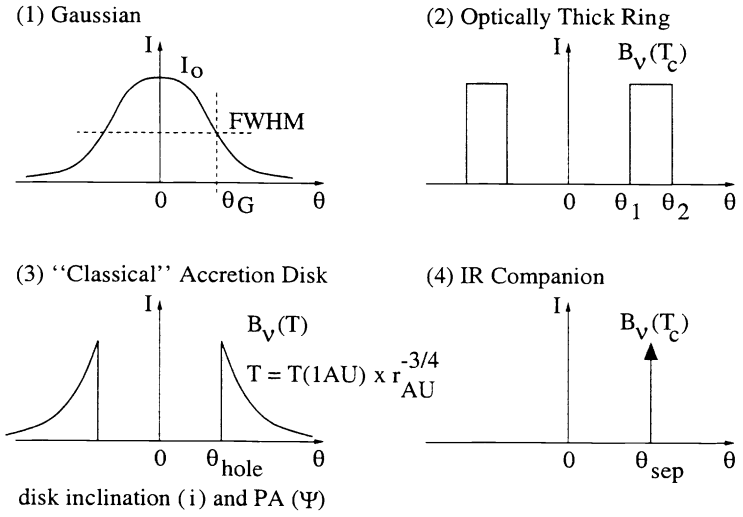

Figure 4. Schematic representation of the four models used to represent the source of IR excess. The free parameters in each case are: (1) Gaussian FWHM θ_G; (2) inner ring diameter θ_1; (3) inner disk diameter θ_{hole}, temperature scale T_{1AU}, disk inclination (i) and disk PA (Ψ); and (4) companion position $\theta_{sep} = (\xi_2, \eta_2)$. T_C is the color temperature of the measured H and K excess.

5.3. Summary of Results

5.3.1. Gaussian intensity

This model is useful in order to set a size scale, and is physically motivated by a CS environment in which the dust particles are distributed in an envelope around the central star.

Table 1 summarizes the results obtained from fitting the visibility data to this model. In addition to the best fitting Gaussian FWHM (θ_G), the table includes the RMS of the fit; the number of individual observations for each star (N); and the linear diameter (D) corresponding to the measured angular diameter. Figure 5 shows the data and models (solid lines) computed with the parameters of Table 1. In this table, and the next, the uncertainties on the sizes derived reflect the systematic uncertainty in the estimate of the photospheric fluxes (30% average), rather than the formal error in fitting the visibility data.

We also calculate in Table 1 the peak brightness temperature (T_B^0), a measure of the peak intensity, determined from the requirement that the flux in the Gaussian matches the excess flux: $I_\nu^0 = F_\nu^E/\Omega_G = B_\nu(T_B^0)$, where $\Omega_G = \pi^2\theta_G^2/4\ln 2$ is the effective solid angle. By comparing the peak brightness temperatures with the color temperatures of the H and K excess (T_C) it is apparent that for most sources the brightness temperature is lower than the color temperature. One possible interpretation is that the near-IR emission is optically thin, in which case the observed color temperature depends on the physical temperature of the dust grains in the source and on their emission properties. In a simple model in which a single temperature characterizes the emission, best agreement with the measured visual extinctions to the stars is obtained under the assumption that the grains in the envelope have neutral opacity (as in large interplanetary dust grains); and the peak optical depths thus derived are in the range $0.03 - 1.2$ (average 0.4).

Table 1. Gaussian model parameters.

Name	θ_G (mas)	FitRMS (%)	N	D (AU)	H-Band T_B^0 (K)	K′-Band T_B^0 (K)	T_c (K)
V594 Cas	≤ 0.8	···	6	≤ 0.5	≥ 1938	$\geq 2212^b$	1382 ± 117
AB Aur	4.1 ± 0.5	4.6	47	0.6 ± 0.1	1359 ± 65	1258 ± 63	1814 ± 331
T Ori	≤ 1.4	···	2	≤ 0.6	≥ 1443	$\geq 1424^b$	1503 ± 110
V380 Ori-A	2.4 ± 0.1	2.0	8	1.1 ± 0.05	1208 ± 22	1144 ± 20^b	1457 ± 113
MWC 147-A	≤ 1.0	···	9	≤ 0.8	≥ 1765	≥ 1884	1467 ± 189
MWC 166-A	≥ 4.5	···	8	≥ 5.2	≤ 1003	$\leq 916^b$	1408 ± 1690
MWC 863-A	7.6 ± 1.7	6.7	18	1.1 ± 0.3	963 ± 44	865 ± 21	1471 ± 405
MWC 275	$4.6^{+1.7}_{-0.8}$	2.8	9	$0.6^{+0.2}_{-0.1}$	1175 ± 104	1124 ± 104^b	1393 ± 375
MWC 297	$5.8^{+0.9}_{-0.5}$	2.0	10	$2.6^{+0.4}_{-0.2}$	1500 ± 77	1594 ± 92^b	1268 ± 143
MWC 614	$7.6_{-2.5}$	2.0	13	$1.8_{-0.6}$	923 ± 74	826 ± 70^b	1453 ± 387
V1295 Aql	$5.4_{-1.4}$	4.3	4	(a)	991 ± 78	910 ± 68^b	1325 ± 424
V1685 Cyg	2.6 ± 0.1	2.8	3	2.5 ± 0.1	1284 ± 30	1235 ± 30^b	1463 ± 126
MWC 1080-A	2.7 ± 0.2	4.9	12	5.9 ± 0.2	1566 ± 33	1535 ± 35	1673 ± 151

Notes:
(a) No distance information is available.
(b) No K-band data available, calculated from size given by H-band data.

5.3.2. Ring model

This model is motivated by the desire to find a structure which is consistent with the effective sizes measured by the interferometer and with thermal emission at the color temperature of the H and K excess.

The results of fits to this model are shown in Table 2. Figure 5 shows the data and models (dot-short dash lines) computed with the parameters of Table 2. We note that the source V594 Cas (which appears unresolved) can not

be represented by this model, due to the fact that for any inner ring diameter, the outer diameter required to match the excess flux results in a source that would appear resolved. Similarly, the large excess flux for MWC 297 implies that any solution for the ring model has a large size, so that the data can formally be well fit only at the peak of the second lobe of the ring visibility function, and we do not consider this a likely interpretation of the data for this source.

Table 2. Ring model parameters.

Name	θ_1 (mas)	FitRMS (%)	N	$\theta_2^{(a)}$ (mas)	D_1 (AU)	D_2 (AU)
V594 Cas	(b)	...	...	...	...	...
AB Aur	4.2 ± 0.4	5.2	47	4.7 ± 0.4	0.6 ± 0.05	0.7 ± 0.05
T Ori	≤ 1.4	...	2	≤ 2.05	≤ 0.6	≤ 0.9
V380 Ori-A	2.5 ± 0.1	2.0	8	3.0 ± 0.1	1.15 ± 0.50	1.4 ± 0.05
MWC 147-A	≤ 0.4	...	12	≤ 2.0	≤ 0.3	≤ 1.6
MWC 166-A	$9.4_{4.5}$	2.5	8	$9.5_{4.4}$	$10.8_{5.2}$	$10.9_{5.1}$
MWC 863-A	$8.2^{+2.7}_{-1.5}$	6.2	18	$8.5^{+2.7}_{-1.5}$	$1.2^{+0.4}_{-0.2}$	$1.3^{+0.4}_{-0.2}$
MWC 275	$4.7^{+1.7}_{-0.9}$	3.1	9	$5.7^{+1.4}_{-0.8}$	$0.6^{+0.2}_{-0.1}$	$0.7^{+0.2}_{-0.1}$
MWC 297[a]	$21.9^{+1.2}$	4.1	10	$25.0^{+1.0}$	$9.9^{+0.5}$	$11.25^{+0.45}$
MWC 614	6.7 ± 1.5	2.3	13	6.9 ± 1.4	1.6 ± 0.4	1.7 ± 0.3
V1295 Aql	$5.4_{-1.2}$	4.4	4	$5.8_{-1.1}$	(b)	(c)
V1685 Cyg	2.7 ± 0.15	2.8	3	3.4 ± 0.15	2.55 ± 0.15	3.3 ± 0.15
MWC 1080-A	2.3 ± 0.3	9.0	20	3.6 ± 0.3	5.1 ± 0.7	7.9 ± 0.7

Notes:
(a) Derived from θ_1 and excess flux.
(b) No solution can match flux and visibility data simultaneously, see text.
(c) No distance information is available.
(d) The only formal solution requires $\theta_1 \gg \theta_G$, see text.

5.3.3. Accretion disk

Given that the stars in our sample which the interferometer resolves are all Group I sources in the classification of HSVK, we consider in this section whether such an accretion disk model is consistent with the interferometer data.

For a flat, thin disk heated by and actively accreting onto a central star, energy balance results in a temperature law which, for $R_\star/r \ll 1$, has the form $T(r) = T_{1AU} \cdot r^{-3/4}$. Having specified a radial temperature law, the SED and visibility curves may be computed by adding the contributions, starting at a minimum radius R_{hole}, from blackbody annuli at temperature $T(r)$.

For every value of the disk inclination (i), the SED completely determines the best fit values of R_{hole} and T_{1AU}, since the flux lost to the lower apparent surface area is recovered by increasing the disk temperature, and the characteristic dip in the shape of the SED in the near-IR is matched by increasing the size of the inner hole. Having found R_{hole} and T_{1AU} such that the SED is well fit for every disk inclination, our approach is to determine the smallest inclination for which there exists a disk position angle (Ψ) such that the visibility data is also well fit.

The results of the detailed calculations show that in most cases this model is ruled out by our data. For most sources, the reason is that the large size measured, and the SED, can not be simultaneously reproduced for any value of the inclination, or require very large inclinations. In other cases (such as AB Aur), although a non-zero inclination results in sources of elliptical shape which can reproduce the large amount of resolution observed by aligning the disk semi-major axis with the IOTA baseline, it also predicts, in contradiction with the data, visibilities that vary with baseline position angle.

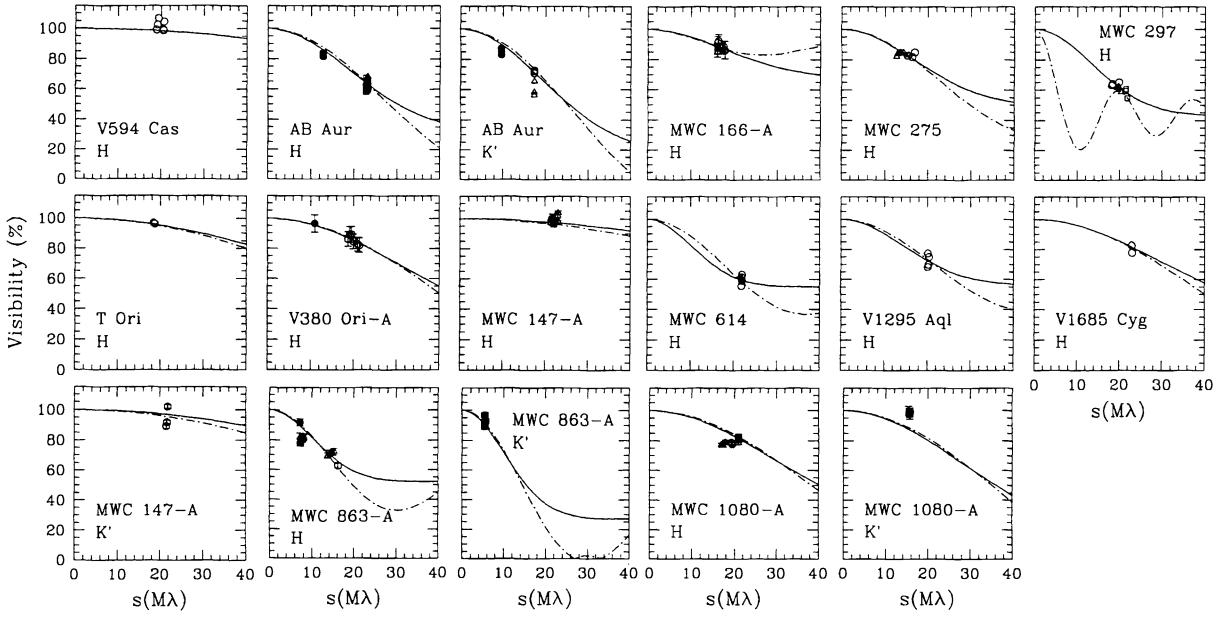

Figure 5. Visibility data and Gaussian and ring models. Solid lines: Point source plus Gaussian intensity model. Dot-short dashed lines: Point source plus uniform ring model.

These conclusions are summarized in Table 3. We find that 6 sources can be successfully fit with the accretion disk model. Of those, 2 are unresolved by the IOTA and are consistent with a face-on disk. The other 4 successful fits (shown in Figure 6) correspond to resolved sources, and 3 of them require extreme values of the disk inclination ($i \geq 80°$). Based on this statistically unlikely requirement, we consider the accretion disk a less attractive explanation for the observed emission*.

Table 3. Accretion disk model parameters.

Name	i (°)	R_{hole} (AU)	T_{1AU} (K)	Ψ (°)	Good Fit to Visibility Data?	FitRMS (%)	$T(R_{hole})$ (K)
V594 Cas	...	...	...	...	No[a]	...	...
AB Aur	...	...	...	...	No	...	...
T Ori	0	0.17	540	any	Yes[a]	0.5	2040
V380 Ori-A	80	0.41	1300	30	Yes	2.5	2537
MWC 147-A	0	0.30	910	any	Yes[a]	4.1	2245
MWC 863-A	...	...	...	...	No	...	...
MWC 275	85	0.24	720	0	Yes	2.1	2100
MWC 297	0	0.90	1830	any	Yes	2.5	1980
MWC 614	...	...	...	...	No	...	...
V1685 Cyg	85	1.05	2500	20	Yes	2.2	2410
MWC 1080-A	...	...	...	...	No	...	...

Notes:
(a) Unresolved.

*The third Group I unresolved source, V594 Cas, is the exception in that the large near-IR excess implies that the closest, but not acceptable, fit is found for a highly tilted disk with its *small* axis oriented along the projected baseline.

We note that, alternatively to tilting the disks, the visibility data may be matched by considering a much steeper temperature law in the inner edge of the disk ($T \propto r^{-8}$, similar to the ring model), so that the H and K′ emission arise essentially from the same radius. Thus, if an accretion disk is the explanation for the near-IR excess, its inner structure must be quite different from the generally accepted range of power law models.

We also note that the inclination angles derived for AB Aur and MWC 275 from mm-wave aperture synthesis observations,[19] 76° and 58° respectively, are inconsistent with our results. Therefore, if the mm-wave data do imply circumstellar disk geometry, the inner disk ($< 1\,AU$) does not follow a simple extrapolation from the disk structure at hundreds of AU from the star.

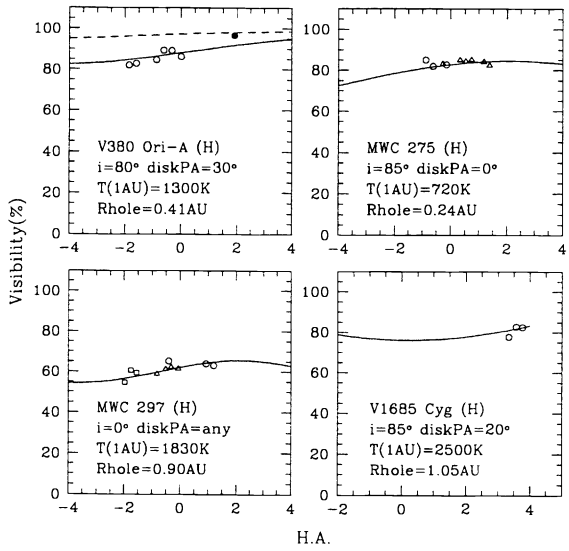

Figure 6. Visibility data and point source plus accretion disk model for the 4 resolved sources which could be successfully fit. The data and models are plotted as a function of source hour angle (H.A.), which determines the orientation of the projected baseline. Note that 3 of the fits require very large values of the disk inclination angle (0° is face-on).

5.3.4. IR Companion

The potential of an infrared companion for reproducing the observed SEDs of HAEBE stars has been previously recognized.[8] In this scenario, the companion is embedded in a dust envelope and appears as an infrared source. Although the only star for which a clear binary detection has been made is MWC 361-A, we must consider the possibility that the other stars appear resolved because we have sampled a few points of what is really the sinusoidal visibility curve of a binary system.

In general, four parameters describe the visibility function for a binary system. These are: The companion angular offsets, ξ_2 and η_2 (determines the period of the sinusoid), and the products of the fraction of the total flux in each component times their normalized visibility as individual sources, $f_{\nu,i=1,2} = V_{\nu,i} \cdot F_{\nu,i}/F_{\nu,1} + F_{\nu,2}$ (determines the amplitude of the sinusoid). Therefore, unless the data provides good coverage in baseline coordinates, further assumptions are needed in order to properly constrain a binary model. In this respect, we have divided our fits to binary models into three categories:

1. Data obtained under essentially a constant baseline position angle. In this case, we assume that both components are unresolved and that the near-IR excess is entirely due to the companion. Furthermore, the binary separation projected along the baseline vector is fit, rather than the true companion position.

2. Data obtained under a significant range of baseline position angle, but the measured visibilities are constant. Here, we also assume that the totality of the near-IR excess is due to the companion, and that both components are unresolved. In these cases, however, the lack of visibility variation provides a useful constraint to the range of possible companion positions, and therefore we derive the range of angular offsets ξ_2 and η_2 that are consistent with the data.

3. MWC 361-A. For this source, the visibility data shows the clear signature of a binary system, detected interferometrically for the first time. Observations were made at two epochs, June 1998 and September 1998; and both H and K′ band data were obtained in each epoch. It may be seen from the data that, because the maximum visibility is less than 100%, a solution where at least one of the components is resolved is required.

In summary, we find that a binary model can be ruled out for AB Aur, since there is no solution that reproduces the constant visibility observed on this source over the 45° range of baseline rotation. For the other sources, a binary model can potentially explain the visibility data. The fit residuals are somewhat smaller than in the case of the Gaussian and ring models, as one would expect since there are more free parameters in the model. However, the difference is within the expected calibration errors and we do not believe it to be significant. For MWC 166-A, the solution with smallest angular offsets corresponds to a separation of $\sim 0.1''$, and it is thus unlikely that such companion would have been un-detected in previous adaptive optics surveys.[20]

The best fit model found for MWC 361-A is shown in Figure 7. Note that we find slightly different companion positions at each epoch. However, the difference is at the 2σ level, and therefore only of marginal significance. We note that from line spectroscopy, the presence of a close companion in this system was previously suspected.[21] Therefore, if it is the star responsible for the radial velocity variations that we have detected interferometrically, this system is a prime candidate for continued observations, using both techniques, from which a full orbital solution and individual stellar masses may be obtained.

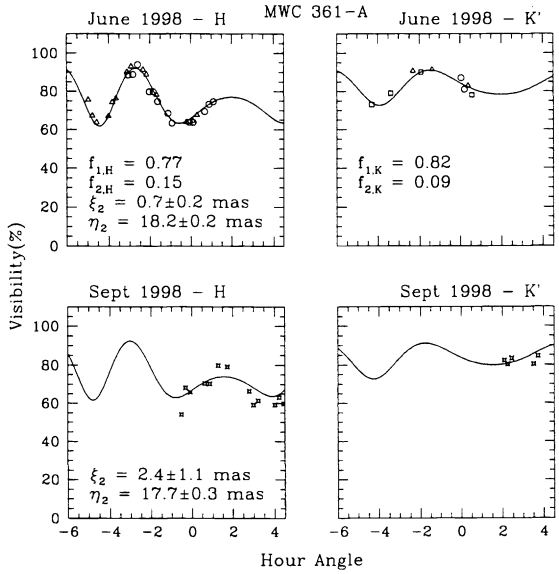

Figure 7. Binary solution for MWC 361-A.

6. DISCUSSION

The results of our study have demonstrated that, contrary to previous belief, most HAEBE stars are easily resolvable in the near-IR by the current class of ground based interferometers. Thus, the question of the precise distribution of CS material in these young stars is one that can potentially be solved using this technique.

It is a striking feature of our data set that, except for the obvious binary, none of the sources shows any departure from a brightness distribution that appears circularly symmetric on the sky. This statement is most significant for sources which have observations on spanning range of baseline position angles. Although the rotation of the baseline is essentially zero in some sources, a more typical value is $\sim 30°$, with a maximum of 65° in the greatest case. Thus, to be consistent with the ensemble of observations, models in which the emitting dust is distributed symmetrically around the star are favored. Physically this would correspond to a spherical distribution of dust, as in the models of Refs. 12,8,9,13. In the context of the Gaussian model we note that the measured sizes, when combined with the derived near-IR fluxes, require the emission to be optically thin, consistent with the fact that the central stars need to be optically visible when viewed through these envelopes. The ring model in this scenario would then interpreted to represent emission from a thin spherical shell, as has been proposed for AB Aur in Ref. 22.

With respect to the physical implications of this model, we find that the properties of the excess are not strongly correlated with those of the underlying star. We show in Figure 8 the location of the stellar photospheres for the sources in our sample in the HR diagram, where the sources which were found to be resolved are shown using symbols proportional to the measured linear sizes given by the Gaussian model. It can be seen that although there is a tendency for the excess sources with largest sizes and highest brightness to be located in the upper left part of the diagram, the dependence of those two quantities with stellar luminosity and effective temperature is rather weak. We also find that there are pairs of sources, (T Ori, V380 Ori-A) and (MWC 147-A, V1685 Cyg), in which the stars and IR excess are essentially identical, but the sources of the IR excesses must differ in size by more than a factor of two. This might suggest that different physical mechanisms are responsible for the near-IR emission in these cases, and that there is no single phenomenon which scales with the properties of the central star or the magnitude of the excess in a simple way. Alternatively, if the same underlying mechanism is at work in all cases, then it must have the property that the same IR excess is produced by systems with different physical scales.

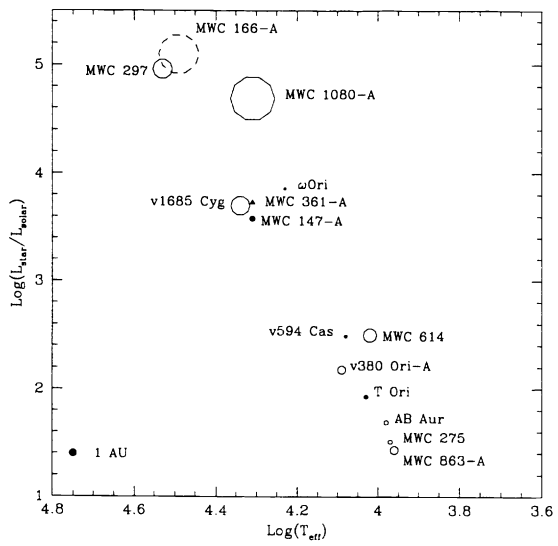

Figure 8. Our sample in the HR diagram. The values plotted correspond to the central photospheres, and the size of each symbol is proportional to the measured linear size of the source of near-IR excess. Solid symbols proportional to the upper limits are used for unresolved sources, and open symbols represent resolved sources (in dashed lines if the size is a lower limit). Different symbols are used for ω Ori (square) because it has no IR excess and for MWC 361 (triangle) because it is a binary system.

REFERENCES

1. G. H. Herbig, "The spectra of Be and Ae type stars associated with nebulosity," *Astrophys. J., Suppl. Ser.* **4**, p. 337, 1960.
2. S. E. Strom, K. M. Strom, J. Yost, L. Carrasco, and G. Grasdalen, "The nature of the Herbig Ae and Be type stars associated with nebulosity," *Astrophys. J.* **173**, p. 353, 1972.
3. M. Cohen and L. V. Kuhi, "Observational studies of pre-main sequence evolution," *Astrophys. J., Suppl. Ser.* **41**, p. 743, 1979.
4. M. E. van den Ancker, D. de Winter, and H. R. E. T. A. Djie, "Hipparcos photometry of Herbig Ae/Be stars," *Astron. Astrophys.* **330**, p. 145, 1998.
5. F. Palla and S. W. Stahler, "The evolution of intermediate-mass protostars. I - Basic results," *Astrophys. J.* **375**, p. 288, 1991.
6. U. Finkenzeller and I. Jankovics *Astron. Astrophys. Suppl. Ser.* **57**, p. 285, 1984.
7. U. Finkenzeller, "Rotational velocities, spectral types, and forbidden lines of Herbig Ae/Be stars," *Astron. Astrophys.* **151**, p. 340, 1985.
8. L. Hartmann, S. J. Kenyon, and N. Calvet, "The excess infrared emission of Herbig Ae/Be stars - Disks or envelopes?," *Astrophys. J.* **407**, p. 219, 1993.
9. A. Miroshnichenko, Ž. Ivezić, and M. Elitzur, "On protostellar disks in Herbig Ae/Be stars," *Astrophys. J., Lett.* **475**, p. L41, 1997.
10. A. Miroshnichenko, Ž. Ivezić, D. Vinković, and M. Elitzur, "Dust emssion from Herbig Ae/Be stars: evidence for disks and envelopes," *Astrophys. J., Lett.* **520**, p. L115, 1999.
11. L. A. Hillenbrand, S. E. Strom, F. J. Vrba, and J. Keene, "Herbig Ae/Be stars: Intermediate-mass stars surrounded by massive circumstellar accretion disks," *Astrophys. J.* **397**, pp. 613–643, 1992.
12. F. Berrilli, G. Corciulo, G. Ingrosso, D. Lorenzetti, and B. Nisini, "Infrared emission from dust structures surrounding Herbig Ae/Be stars," *Astrophys. J.* **398**, p. 2254, 1992.
13. S. Pezzuto, F. Strafella, and D. Lorenzetti, "On the circumstellar matter distribution around Herbig Ae/Be Stars," *Astrophys. J.* **485**, p. 290, 1997.
14. A. Natta, F. Palla, H. M. Butner, N. J. Evans, and P. M. Harvey, "Infrared studies of circumstellar matter around Herbig Ae/Be and related stars," *Astrophys. J.* **406**, p. 674, 1993.
15. W. A. Traub, "Recent results from the IOTA interferometer," in *Proc. SPIE 3350: Astronomical Interferometry*, R. D. Reasenberg and J. B. Breckinridge, eds., p. 848, 1998.
16. R. Millan-Gabet, F. P. Schloerb, W. A. Traub, and N. P. Carleton, "A NICMOS3 camera for fringe detection at the IOTA interferometer," *Publ.. Astron. Soc. Pac.* **111**, p. 238, 1999.
17. R. Millan-Gabet, *Investigation of Herbig Ae/Be Stars in the Near-Infrared with a Long Baseline Interferometer*. PhD thesis, University of Massachusetts at Amherst, USA, 1999. Available on the www at: http://cfa-www.harvard.edu/~rmillan/.
18. P. S. Thé, D. de Winter, and M. R. Perez, "A new catalogue of members and candidate members of the Herbig Ae/Be (HAEBE) stellar group," *Astrophys. J., Suppl. Ser.* **104**, pp. 315–339, 1994.
19. V. Mannings and A. Sargent, "A high resolution study of gas and dust around young intermediate-mass stars: Evidence for circumstellar disks in Herbig Ae systems," *Astrophys. J.* **490**, pp. 792–802, 1997.
20. P. Corporon, *La binarite des etoiles Ae/Be de Herbig vue par l'optique adaptative et par la spectroscopie. Une etude de systeme triple TY CrA*. PhD thesis, Université Joseph Fourier de Grenoble, France, 1998.
21. P. Corporon and A. M. Lagrange, "A search for spectroscopic binaries among Herbig Ae/Be stars," *Astron. Astrophys.* **136**, p. 429, 1999.
22. H. M. Butner *et al.*, "Density profiles of the envelopes surrounding Herbig Ae/Be stars," in *The nature and evolutionary status of Herbig Ae/Be stars*, P. S. Thé, ed., p. 185, A. S. P. Conference Series Vol. 62, 1994.